HHS Public Access

Author manuscript

Cell Rep. Author manuscript; available in PMC 2021 July 14.

Published in final edited form as:

Cell Rep. 2021 July 06; 36(1): 109315. doi:10.1016/j.celrep.2021.109315.

Patient-derived iPSC-cerebral organoid modeling of the 17q11.2 microdeletion syndrome establishes *CRLF3* as a critical regulator of neurogenesis

Michelle L. Wegscheid[1], **Corina Anastasaki**[1], **Kelly A. Hartigan**[1], **Olivia M. Cobb**[1], **Jason B. Papke**[1], **Jennifer N. Traber**[1], **Stephanie M. Morris**[1], **David H. Gutmann**[1,2,*]

[1]Department of Neurology, Washington University School of Medicine, St. Louis, MO 63110, USA

[2]Lead contact

SUMMARY

Neurodevelopmental disorders are often caused by chromosomal microdeletions comprising numerous contiguous genes. A subset of neurofibromatosis type 1 (NF1) patients with severe developmental delays and intellectual disability harbors such a microdeletion event on chromosome 17q11.2, involving the *NF1* gene and flanking regions (*NF1* total gene deletion [*NF1*-TGD]). Using patient-derived human induced pluripotent stem cell (hiPSC)-forebrain cerebral organoids (hCOs), we identify both neural stem cell (NSC) proliferation and neuronal maturation abnormalities in *NF1*-TGD hCOs. While increased NSC proliferation results from decreased *NF1*/RAS regulation, the neuronal differentiation, survival, and maturation defects are caused by reduced cytokine receptor-like factor 3 (*CRLF3*) expression and impaired RhoA signaling. Furthermore, we demonstrate a higher autistic trait burden in NF1 patients harboring a deleterious germline mutation in the *CRLF3* gene (c.1166T>C, p.Leu389Pro). Collectively, these findings identify a causative gene within the *NF1*-TGD locus responsible for hCO neuronal abnormalities and autism in children with NF1.

Graphical Abstract

*Correspondence: gutmannd@wustl.edu.

AUTHOR CONTRIBUTIONS

M.L.W. and D.H.G. designed the experiments. M.L.W., K.A.H., O.M.C., C.A., S.M.M., and J.B.P. conducted the experiments and/or analyzed the data. S.M.M. and J.N.T. collected patient specimens. The manuscript was assembled by M.L.W. and D.H.G. D.H.G. was responsible for the final production of the manuscript.

SUPPLEMENTAL INFORMATION

Supplemental information can be found online at https://doi.org/10.1016/j.celrep.2021.109315.

DECLARATION OF INTERESTS

The authors declare no competing interests.

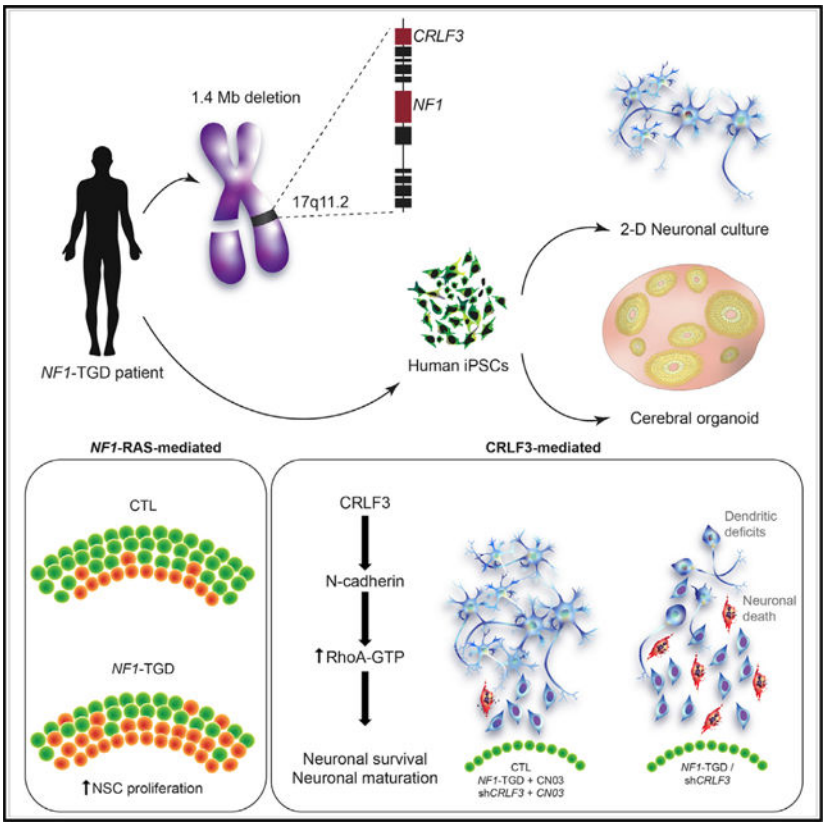

In brief

To critically evaluate the impact of *NF1* locus genomic microdeletion (17q11.2) on the development of human brain cells, Wegscheid et al. generated patient-derived hiPSC forebrain cerebral organoids (hCOs). Although increased hCO neural stem cell proliferation is RAS-dependent, the neuronal survival, differentiation, and maturation defects resulted from reduced *CRLF3*-dependent RhoA activation.

INTRODUCTION

Neurodevelopmental disorders (NDDs) comprise a diverse collection of syndromes in which affected children exhibit autism spectrum symptomatology, cognitive delays, and intellectual disabilities. Genomic sequencing and chromosomal analyses have revealed that many NDDs are associated with chromosomal copy number variations (CNVs) (Coe et al., 2019; Grayton et al., 2012), leading to altered expression of specific genes. As such, microdeletion syndromes have been highly instructive for identifying pathology-causing genes, as well as dissecting the underlying mechanisms responsible for these neurodevelopmental abnormalities (Frega et al., 2019; Pucilowska et al., 2018; Ramocki et al., 2010; Shcheglovitov et al., 2013).

Microdeletions on chromosome 17q11.2 most commonly encompass 1.4 Mb of genomic DNA, including the entire *NF1* gene and its flanking regions (type 1 *NF1*-total gene deletion [*NF1*-TGD]). These microdeletion events are found in 4.7%–11% of patients with

neurofibromatosis type 1 (NF1) (MIM: 162200) (Kluwe et al., 2004; Rasmussen et al., 1998), where children with *NF1*-TGD mutations manifest profound developmental delays, intellectual disability (IQ < 70), and an elevated risk of cancer (Descheemaeker et al., 2004; Mautner et al., 2010; Ottenhoff et al., 2020; Pasmant et al., 2010; Venturin et al., 2004). While it is possible that these clinical abnormalities result from the total deletion of one copy of the *NF1* gene, the *NF1*-TGD locus contains 13 other protein-coding and 4 microRNA genes, which could also contribute to these manifestations. To this end, only the deletion of one of these genes, *SUZ12*, has been previously correlated with the increased cancer incidence in these patients (De Raedt et al., 2014; Lee et al., 2014; Wassef et al., 2019; Zhang et al., 2014). In contrast, the underlying molecular etiologies for the neurodevelopmental deficits in this population are unknown.

To define the molecular and cellular cause(s) for the neurodevelopmental abnormalities in patients with 17q11.2 microdeletions, we established human induced pluripotent stem cell (hiPSC)-forebrain cerebral organoid (hCO) models from several NF1 patients with a 1.4-Mb *NF1*-TGD mutation (TGD hCOs). Leveraging this platform, we identified neuronal survival, differentiation, and maturation abnormalities in the TGD hCOs, which were not observed in hCOs harboring intragenic *NF1* mutations or an atypical deletion (aTGD). Using a number of converging strategies, we identified a single gene (*CRLF3*) and signaling pathway (RhoA activation) responsible for the neuronal maturation defects observed in TGD hCOs. Moreover, we demonstrated a higher autistic trait burden in NF1 patients harboring a deleterious germline mutation in the *CRLF3* gene (p.Leu389-Pro). Collectively, these experiments reveal a causative gene and mechanism responsible for the profound neurodevelopmental abnormalities of TGD hCOs.

RESULTS

TGD hCOs have neuronal defects

Using hCOs from three neurologically normal control individuals and three individuals harboring a 1.4-Mb *NF1*-TGD (Figures 1A and S1A–S1E; Table S1), we first assessed neural stem cell (NSC) proliferation. Similar to hCOs harboring intragenic NF1 patient *NF1* gene point mutations (Anastasaki et al., 2020) (Table S1), TGD hCOs also exhibited increased NSC proliferation (% $Ki67^+$ NSCs per hCO ventricular zone [VZ]) at 16 and 35 days *in vitro* (DIV) (Figures 1B and 1D) and 5-ethynyl-2′-deoxyuridine (EdU) incorporation at 16 DIV (Figure S2A) relative to control hCOs.

Next, to assess the temporal course of neurogenesis in these $PAX6^+/OTX2^+$ dorsal telencephalic forebrain hCOs (Figure S1E), cryosections were immunostained for markers of early-stage ($NeuroD1^+$)- and late-stage ($NeuN^+$) immature neurons, as well as deep-layer ($TBR1^+$) and upper-layer ($SATB2^+$) neurons (Figures 1C and S1G–S1F). The TGD hCOs produced increased numbers of $NeuroD1^+$ immature neurons relative to control hCOs from 16 to 56 DIV (Figure 1E), after which time, $NeuroD1^+$ neurons were no longer present. Late-stage immature $NeuN^+$ neurons and deep-layer $TBR1^+$ neurons were first detected at 35 DIV in both control and TGD hCOs; however, the TGD hCOs had reduced numbers of $NeuN^+$ and $TBR1^+$ neurons (Figures 1F and S1G) at 35 and 56 DIV. Despite normalization of $NeuN^+$ neuronal numbers at 84 DIV (Figure 1H) and no microcephalic defects (Figures

S1B–S1D), the TGD hCOs had reduced numbers of upper-layer SABT2$^+$ neurons at 84 DIV (Figure S1H), demonstrating a persistent imbalance in the neuronal subtypes generated. This impaired neuronal differentiation was unique to the TGD hCOs, as it was not observed in hCOs harboring five distinct intragenic *NF1* gene mutations (Table S1; Figure S2B).

As the increased numbers of early-stage immature neurons in the TGD hCOs did not generate a compensatory increase in late-stage immature neurons, we hypothesized that the TGD NeuroD1$^+$ neurons were being eliminated by programmed cell death. To measure apoptosis, 35 and 56 DIV hCOs were immunolabeled for the early-stage (cleaved caspase-3) and late-stage (TUNEL) apoptotic markers, respectively. Greater caspase-3 cleavage (11.8% increase; Figures 1G and 1H) and DNA fragmentation (6.3% TUNEL increase; Figure S2C) were observed in the TGD NeuroD1$^+$ neurons relative to controls, establishing a concurrent increase in production and apoptosis of early-stage immature neurons in TGD hCOs. The increased apoptosis of NeuroD1$^+$ neurons in TGD hCOs, coupled with differentiation of the remaining NeuroD1$^+$ neurons in TGD hCOs at 56 DIV, accounts for normalization of late-stage immature neurons at 84 DIV.

The finding of neuronal differentiation defects in the TGD hCOs prompted us to determine whether there were also defects in dendrite and axonal extension, as reported in children with autism spectrum disorder (ASD) and intellectual disability (Hutsler and Zhang, 2010; Lazar et al., 2014; Mukaetova-Ladinska et al., 2004; Wolff et al., 2012). While the TGD hCOs produced normal SMI-312$^+$ axonal projections, they had reduced MAP2$^+$ and SMI-32$^+$ dendrites in hCOs from 35 to 84 DIV (Figures 1I, S1F, S2D, and S2E), abnormalities not observed in hCOs harboring intragenic *NF1* mutations (Figure S2F). Similar to TGD hCOs, hiPSC-derived neurons in 2D cultures also exhibited reduced MAP2$^+$ and SMI-32$^+$ dendrites (Figure 1J)

Taken together, these results reveal that TGD hCOs and hCOs harboring intragenic *NF1* mutations have increased NSC proliferation, reflecting impaired *NF1* gene function, but additionally exhibit neuronal abnormalities (dendritic maturation) unique to TGD hCOs.

NSC hyperproliferation in TGD hCOs is RAS-dependent

To further explore the impact of complete *NF1* deletion on NSC proliferation in the absence of other genetic contributors, we generated hCOs from the single available patient-derived hiPSC line harboring a rare atypical (0.6–0.9 Mb) deletion (aTGD), involving the loss of six protein-coding genes, including *NF1*, but not the eight protein-coding genes deleted in the common 1.4-Mb *NF1*-TGD (Figure 2A). Similar to the TGD and intragenic *NF1* mutant hCOs (Anastasaki et al., 2020), the aTGD hCOs had increased NSC proliferation (%Ki67$^+$ NSCs; Figure 2B) relative to controls. Since the *NF1* protein (neurofibromin) has previously been shown to mediate increased cell proliferation through RAS regulation in numerous *NF1*-mutant cell types (Chen et al., 2015; Hegedus et al., 2007; Lee et al., 2010; Sanchez-Ortiz et al., 2014; Wang et al., 2012), we hypothesized that the increased NSC proliferation observed in the *NF1*-mutant hCOs was RAS dependent. Similar to the intragenic *NF1*-mutant hCOs (Anastasaki et al., 2020), TGD and aTGD hCOs had increased RAS activity (1.4- and 2.1-fold, respectively) relative to controls (Figure 2C). To investigate the relationship between RAS hyperactivation and increased NSC proliferation in the *NF1*-

mutant hCOs, we incubated control, TGD, and aTGD hCOs with an experimentally determined concentration of the pan-RAS inhibitor IN-1(IN-1) for 48 h (Figures S3A–S3C). While IN-1 had no effect on NSC proliferation in control hCOs (Figure S3D) or neuronal differentiation and dendrite maturation in TGD and aTGD hCOs (Figures S3E–S3F), it reduced the NSC hyperproliferation in TGD and aTGD hCOs (Figure 2D), confirming that RAS hyperactivation is solely responsible for the increased NSC proliferation observed in *NF1*-mutant hCOs.

TGD hCOs have reduced *CRLF3* expression

In striking contrast to the TGD hCOs, the aTGD hCOs lacked neuronal survival, differentiation, and maturation abnormalities. In this regard, the aTGD hCOs produced normal numbers of late-stage immature neurons (Figure 2E), exhibited no increase in immature neuron apoptosis (Figure 2F), and had normal dendrites (Figure 2G) relative to controls. These observations demonstrate that genes outside of the atypical deletion region are responsible for the neuronal differentiation and maturation defects observed in the TGD hCOs.

To identify the responsible gene(s), we conducted a systematic analysis of the genes contained within the 1.4-Mb deletion region, but not in the atypical deletion region (Figure 3A). First, the deletion status of two genes in the aTGD hCOs (*COPRS* and RAB11FIP4) was assayed by quantitative real-time PCR (Figures 3B and S3G), revealing reduced expression of *RAB11-FIP4* (within the aTGD region), but not *COPRS* (outside the aTGD region). Next, we excluded the three microRNA genes that exhibited highly variable mRNA expression (Figure S3H), as well as one protein-coding gene (*ADAP2*) and one microRNA gene (*MIR4733*), which were not expressed in control hCOs. We then analyzed the differential gene expression of the seven remaining protein-coding genes at an experimentally determined time point where the highest levels of mRNA expression were detected in control hCOs (Figure S3I).

All seven genes had reduced mRNA expression in the TGD hCOs relative to controls (Figure 3B). However, cytokine receptor-like factor 3 (*CRLF3*) was the only gene with reduced protein levels in the TGD hCOs relative to the aTGD and control hCOs (82% and 66%, respectively) (Figures 3B, 3C, and S3J–S3N), implicating *CRLF3* in the neuronal defects observed only in TGD hCOs.

CRLF3 mutation is associated with increased autism trait burden in patients with NF1

To further investigate *CRLF3* as a potential gene involved in neurodevelopment, we evaluated *CRLF3* mutation status in a previously assembled cohort of individuals with NF1 from the Washington University NF Center. We specifically chose patients who underwent Social Responsiveness Scale, Second Edition (SRS-2) testing as part of routine NF1 clinical screening, had DNA banked under an approved Human Studies protocol (Constantino et al., 2015), and were between the ages of 10 and 19, based on the World Health Organization definition of adolescence (World Health Organization, 2017) and previously described age-dependent differences in autistic trait burden in children, adolescents, and adults with NF1

(Morris et al., 2016). After excluding patients with CNVs (n = 1), 17 patients were analyzed (Table S2).

Genomic DNA was whole-exome sequenced (WES) to identify genetic variants, which were prioritized according to their annotated impact (STAR Methods). A single deleterious *CRLF3* missense mutation (c.1166T>C, p.Leu389Pro) affecting a highly conserved amino acid within the CRLF3 protein (Figure S4A) was identified in 7/17 of the NF1 patients (Figure 3D). Grouping of patients by *CRLF3* c.1166T>C mutation status revealed higher SRS-2 scores in NF1 patients with this mutation than in those without it ($p = 0.0374$) (Figure 3E). The neuronal differentiation, survival, and maturation abnormalities in TGD hCOs harboring a heterozygous *CRLF3* deletion, coupled with the observed increase in autistic trait burden in patients harboring a deleterious mutation in the *CRLF3* gene, suggests an essential role for *CRLF3* in human brain development. This notion is further supported by the high amino acid sequence conservation of CRLF3 across vertebrates (Hahn et al., 2017, 2019; Ostrowski and Heinrich, 2018) and enriched *CRLF3* expression found in human embryonic brain tissues (Yang et al., 2009) (Figure S4B).

CRLF3 reduction recapitulates the TGD neuronal defects

To determine whether reduced *CRLF3* expression was responsible for the neuronal maturation defects observed in TGD hCOs, control hiPSCs were infected with four unique *CRLF3* (sh*CRLF3*) and four unique control (shCTL) short hairpin RNA constructs. All four sh*CRLF3* constructs had reduced *CRLF3* expression relative to shCTLs (Figures 4A and S4C). While *CRLF3* reduction had no effect on NSC proliferation (Figure 4B) or neurofibromin protein expression and subcellular localization (Figures S4D–S4F), it fully replicated the neuronal abnormalities observed in the TGD hCOs. In this regard, sh*CRLF3* hCOs had increased numbers of early-stage immature neurons at 16 DIV, reduced numbers of late-stage immature neurons at 35 DIV (Figure 4C), increased immature neuron apoptosis (Figure 4D), and reduced SMI-32^+ dendrites (Figure 4E) and $SATB2^+$ upper layer neurons (Figure S4G) compared to shCTL hCOs. These results demonstrate that reduced CRLF3 expression is sufficient to produce the TGD neurogenic abnormalities, establishing *CRLF3* as a key regulator of human neuron differentiation, survival, and maturation.

CRLF3-mediated dendritic defects result from impaired RhoA activation

To gain mechanistic insights into CRLF3-mediated signaling in human brain cells, we performed RNA sequencing on CTL, TGD, sh*CRLF3*, and aTGD NSCs (Figures 4F, 4G, and S4H). First, we identified differentially expressed genes (DEGs) (p values, false discover rates [FDRs] ≤ 0.01; log-fold changes ≥ ±5) in TGD NSCs relative to CTL and aTGD NSCs. This DEG list was filtered for non-significant genes in the comparison of TGD and sh*CRLF3* NSCs (Table S3). Subsequent gene ontology (GO) enrichment analysis demonstrated δ-catenin binding as the most highly enriched GO term (Figure 4G). Notably, dysregulation of δ-catenin signaling has been implicated in autism (Turner et al., 2015), dendritic spine morphogenesis, maintenance, and function during development (Arikkath et al., 2009; Matter et al., 2009) through regulation of N-cadherin levels (Fukata and Kaibuchi, 2001; Tan et al., 2010) and activation of Rho-family GTPases, RhoA, and Rac1 (Arikkath et al., 2009; Elia et al., 2006; Gilbert and Man, 2016). To determine whether CRLF3 regulates

this pathway in cells and tissues harboring a TGD, we measured N-cadherin protein levels, as well as Rac1 and RhoA activation in CTL, TGD, and sh*CRLF3* NSCs (Figures 4H–4K and S4I–S4K). Consistent with this proposed mechanism, TGD and sh*CRLF3* NSCs had reduced N-cadherin levels (TGD, 65% reduction; sh*CRLF3*, 52% reduction; Figures 4H and S4G), decreased Rac1 activation (TGD, 18.5% reduction; Figure 4I; sh*CRLF3*, 13.1% reduction; Figure S4I), and decreased RhoA activation (TGD, 76.6% reduction; Figure 4J; sh*CRLF3*, 77.1% reduction; Figure 4K) relative to controls. Moreover, treatment of TGD and sh*CRLF3* hCOs with an experimentally determined concentration of the RhoA activator CN03 (Figure S4K) rescued the neuron maturation defect (TGD, 35.8% reduction in NeuroD1, 1.9-fold increase in NeuN; Figure 4J; sh*CRLF3*, 57.7% reduction in NeuroD1, 2.6-fold increase in NeuN; Figures 4L, 4M, and S4L), neuronal apoptosis (TGD, 23% reduction; sh*CRLF3*, 17.6% reduction in Cl. Caspase-3; Figures 4N and S4M), and dendrite maturation defect (TGD, 2.5-fold increase; sh*CRLF3*, 2.6-fold increase in SMI-32 immunopositivity; Figures 4O and S4N), normalizing them to control levels in 35 DIV hCOs. These results establish reduced RhoA signaling as the etiologic mechanism responsible for the impaired neuron maturation and neurite outgrowth in TGD hCOs.

DISCUSSION

The successful deployment of the hCO platform to identify the cellular and molecular etiologies for human 17q11.2 microdeletion-related neurodevelopmental abnormalities raises several important points. First, it adds *CRLF3* to the growing list of genes contained within the *NF1*-TGD locus that could contribute to specific clinical phenotypes observed not only in patients with NF1, but also in the general population. For example, mutations in *RNF135* have been reported in patients with autism (Tastet et al., 2015) and in families with dysmorphic facial features and learning disabilities (Douglas et al., 2007). Biallelic loss of *SUZ12* is frequently observed in malignant peripheral nerve sheath tumors (MPNSTs) (Lee et al., 2014; Zhang et al., 2014), while *ADAP2* is required for normal cardiac morphogenesis (Venturin et al., 2014) relevant to cardiovascular malformations observed in 17q11.2 microdeletion patients (Venturin et al., 2004). Further investigation into the roles of other deleted genes within this interval may provide insights relevant to the diagnosis and treatment of human disease. Second, using a combination of lentiviral *CRLF3* genetic silencing and pharmacologic rescue of RhoA activity experiments (CN03 treatments), we establish that *CRLF3* regulates human neurogenesis, neuron survival, and dendritic development through RhoA activation, extending prior studies on the role of RhoA signaling in murine neuron maturation relevant to neurodevelopment and cognition (Richter et al., 2019). Third, the provocative early-phase clinical analyses suggest that *CRLF3* mutation might identify a high-risk group of NF1 patients more likely to harbor an increased autism trait burden. While *CRLF3* has not been previously implicated as an autism risk gene (Abrahams et al., 2013; Banerjee-Basu and Packer, 2010), it constitutes a potential therapeutic target and a risk assessment tool in future studies involving larger numbers of individuals, with a focus on its sensitivity and specificity for predicting ASD symptomatology in children with NF1.

Limitations of the study

While we show that CRLF3 reduction accounts for the impaired neuronal maturation and dendritic outgrowth in *NF1*-TGD hCOs, further work will be required to establish a link between *NF1*-TGD dendritic dysfunction and autism. Additionally, analysis of an *in vivo* model would be required to validate the translatability of these results. Similarly, as aTGD mutations are quite rare, additional studies should focus on the neuronal function in this subset of TGD patients. Last, with the availability of reliable antibodies that recognize the proteins encoded by other genes in the microdeletion locus and *CRLF3* expression constructs, future studies could explore the relationship between these deleted genes and brain development.

STAR★METHODS

RESOURCE AVAILABILITY

Lead contact—Further information and requests for resources and reagents should be directed to and will be fulfilled by the Lead Contact, Dr. David H. Gutmann (gutmannd@wustl.edu).

Materials availability—hiPSC lines generated for this study are available upon request to Dr. David H. Gutmann.

Data and code availability—This study did not generate any codes. The whole exome sequencing data are available under accession number PRJNA698597 (SRA database). The RNA sequencing data are available in the GEO repository (GSE166080). Any other relevant data are available from the corresponding author upon request.

EXPERIMENTAL MODEL AND SUBJECT DETAILS

Human induced pluripotent stem cells—Patient-derived hiPSC lines were reprogrammed by the Washington University Genome Engineering and iPSC Core Facility (GEiC) using biospecimens (skin, blood, urine) acquired from three individuals harboring a 1.4 Mb *NF1*-total gene deletion (TGD) and one patient harboring an atypical TGD (aTGD) (Table S1) with an established diagnosis of NF1 under an approved Human Studies Protocol at Washington University. As atypical TGD mutations are rare in the NF1 population (Messiaen et al., 2011), no additional patients with this genomic alteration were available to generate hiPSC lines. Briefly, fibroblasts, renal cells or peripheral blood cells were infected with a Sendai virus carrying four stem cell reprogramming factors (*OCT4*, *KLF4*, *SOX2*, *C-MYC*), as previously reported (Anastasaki et al., 2015, 2020). hiPSC colonies were isolated and pluripotency was confirmed by morphological assessment and expression of stem cell markers (Figure S1A). Two to three different clones were expanded for each line, tested and verified negative for *Mycoplasma* contamination, and used to generate human cerebral organoids (hCOs) (Figures S1B–S1E), neural progenitor cells (NSCs) (Figure S4E) and neurons. The sizes of the *NF1* locus deletions were determined by MLPA assay (MRC Holland) at the Medical Genomics Laboratory (University of Alabama, Birmingham). Single clones of two patient-derived neurologically normal controls were provided by Drs. Matthew B. Harms (CTL2, male) and Fumihiko Urano (CTL3, male) at Washington University. Five

distinct isogenic human induced pluripotent stem cell (hiPSC) lines harboring NF1 patient germline *NF1* gene mutations (Transcript ID NM_000267; c.1149C > A, c.1185+1G > A, c.3431–32_dupGT, c.5425C > T, c.6619C > T) were individually engineered into a single commercially available male control human iPSC line (BJFF.6, CTL1) as previously described (Anastasaki et al., 2020) (Table S1). All hiPSC lines generated by CRISPR/Cas9 engineering were subjected to subcloning and Illumina deep sequencing to verify the presence of the introduced mutation. These renewable resources are continuously frozen at low passage (< 5). All hiPSC clones were used for analysis and relative to prior frozen aliquots of the same clone to ensure reproducibility. hiPSCs have been authenticated by (a) routine testing for *Mycoplasma* infection, (b) regular quality control checks for pluripotency by monitoring expression of pluripotency markers, and (c) competence to undergo multi-lineage differentiation.

Human subject details—Samples for exome sequencing were acquired from a previously assembled cohort of individuals with NF1 from Washington University Neurofibromatosis Center whose DNA was banked under a Human Studies protocol approved by the Washington University Human Research Protection Office (Constantino et al., 2015). Informed consent was obtained from all participants. Patients with copy number variants (CNVs) (n = 1) were excluded. Of the patients between 10 and 19 years of age with clinically indicated SRS-2 testing, 11 were male (64.7%) and 6 were female (35.3%). Selected individuals ranged in age from 10 to 18 years (median, 13 years), with SRS-2 T scores from 45 to 98 (Table S2). There was no significant difference between males (n = 11) and females (n = 6) with respect to SRS-2 scores, between males (n = 5) and females (n = 2) in the group with a deleterious p.Leu389Pro *CRLF3* mutation (n = 7), or between males (n = 6) and females (n = 4) without a *CRLF3* mutation (n = 10).

METHOD DETAILS

Human iPSC, cerebral organoid, NSC and 2D neuron cultures—hiPSCs were cultured on Matrigel (Corning)-coated culture flasks and were fed daily with mTeSR Plus (05825, STEMCELL Technologies). hiPSCs were passaged with ReLeSR (05873, STEMCELL technologies) following manufacturer's instructions. hCOs were generated as previously described (Anastasaki et al., 2020). Briefly, cerebral organoids were cultured from hiPSCs by first aggregating 40,000 hiPSCs per well of an ultra-low binding 96-well U-bottom plate (Corning) to allow for embryoid body (EB) formation. EBs were fed every other day with STEMdiff Neural Induction Medium (05835, STEMCELL technologies) supplemented with low concentration bFGF (4ng/mL; 100-18B, PeproTech) and ROCK inhibitor (20 μM; Y27632, Millipore) for the first 6 days, followed by NIM minus bFGF and ROCK inhibitor for an additional 3 days. Tissues were then transferred to Corning Costar 24 Well Clear Flat Bottom Ultra Low Attachment plates (1 organoid per well) in hCO differentiation medium (125 mL DMEM-F12, 125 mL Neurobasal medium, 1.25 mL N2 supplement, 62.5 μl insulin, 2.5 mL GlutaMAX supplement, 1.25 mL MEM-NEAA, 2.5 mL B27 supplement, 2.5 mL penicillin-streptomycin, 87.5μl of a 1:100 dilution of 2-mercaptoethanol in DMEM-F12) on an orbital shaker rotating at 80 rpm. hCO differentiation media was changed every 3 days. hCOs were maintained for up to 84DIV. Neural progenitor cells (NSCs) were generated using previously described methods

(Anastasaki et al., 2020). For non-specific neuronal differentiation, NSCs were cultured in PLO/Laminin-coated plates in neuronal differentiation media (490 mL Neurobasal media, 5 mL N2 supplement, 5 mL MEM-NEAA) supplemented with 0.01 μg/ml BDNF (450-02, PeproTech), IGF-I (100-11, PeproTech), GDNF (78058, STEMCELL technologies), cAMP (1μM; 1698950, PeproTech), and Compound E (0.2 μM; 73954, STEMCELL technologies) for 7 days.

Whole exome sequencing—Genomic DNA samples were whole exome sequenced (Otogenetics Ltd), and FASTQ files aligned to the human reference genome assembly (GRCh37/hg19) using Samtools 1.4.1 software. Sequence variants of *CRLF3* were called, filtered, and prioritized according to their impact annotation obtained from SnpEff. Pathogenicity of resulting variants was additionally confirmed using CADD, SIFT, PolyPhen, likelihood ratio test (LRT), GERP++, and Fathmm.

Next generation RNA sequencing and analysis—RNA sequencing (RNA-seq) was performed on CTL1, CTL2, TGD1, TGD2, TGD3, aTGD and sh*CRLF3*-1 NSCs as previously described (Anastasaki et al., 2020). Sequencing analyses were generated using Partek Flow software, version 9.0.20 (Partek Inc, 2020). RNA-seq reads were aligned to the Ensembl transcripts release 100 top-level assembly with STAR version 2.7.3a (Dobin et al., 2013). Gene counts and isoform expression were derived from Ensembl output. Sequencing performance was assessed for the total number of aligned reads, total number of uniquely aligned reads, and features detected. Normalization size factors were calculated for all gene counts by median ratio. Differential genetic analysis was then performed using DESeq2 (Love et al., 2014) to analyze for differences between conditions. Results for TGD samples compared separately with CTLs and aTGD samples were filtered for only those genes with *P value*s and false discovery rates (FDR) ≤ 0.01 and log fold-changes ≥ ± 5. This gene list was then filtered further for only non-significant genes in the comparison of TGD samples versus sh*CRLF3* samples. This resulted in a gene list of 31 genes (Table S3). Gene Ontology enrichment (Ashburner et al., 2000) was run on the resulting gene list. Deep sequencing data is in the process of being submitted to GEO.

Immunohistochemistry—hCOs were fixed, embedded and cryosectioned at 12 μm as previously described (Sloan et al., 2018). Tissues were permeabilized in 0.5% Triton X-100 in PBS for 5 minutes. After three PBS washes, tissues were blocked in a solution of 10% goat serum (GS) in PBS for one hour at room temperature, then immunolabeled with primary antibodies, diluted in a solution of 2% GS, overnight at 4°C. The following primary antibodies were used: anti-SOX2 (1:400, 4900, Cell Signaling Technology), anti-SOX2 (1:200, ab92494, Abcam), anti-OCT4A (1:400, 2840, Cell Signaling Technology), anti-NANOG (1:800, 3580, Cell Signaling Technology), anti-SMI-32 (2.5 μg/mL, 801701, Biolegend), anti-SMI-312 (2.5 μg/mL, 837904, Biolegend), anti-NeuroD1 (1:250, ab205300, Abcam), anti-NeuroD1 (1:500, ab60704, Abcam), anti-NeuN (1:500, MAB377, Millipore), anti-Ki67 (1:100, BD556003, BD Biosciences), anti-MAP2 (1:500, ab11267, Abcam), anti-cleaved caspase-3 (1:250, 9664, Cell Signaling Technology), anti-active caspase-3 (1:100, AF835, R&D systems), anti-PAX6 (1:250, ab19504, Abcam), anti-OTX2 (1:200, MA5-15854, Thermo Fisher Scientific), anti-EN1 (1:50, PA5-14149, Thermo Fisher

Scientific), anti-GBX2 (1:50, LS-C197281, Lifespan Biosciences), anti-TBR1 (1:200, ab31940, Abcam), anti-SATB2 (1:100, ab51502, Abcam), anti-Vimentin (1:100, 5741, Cell Signaling Technology), anti-Nestin (1:250, ab92391, Abcam). The following day, slides were washed three times with PBS and labeled with relevant secondary antibodies [AlexaFluor488/568 (1:200, Invitrogen)] for one hour at room temperature. Hoechst (1:5000 in PBS) was used for cell nucleus staining. For EdU pulse-chase analyses, 16DIV hCOs were incubated with 10 μM EdU for 1.5 hours. EdU staining was performed using Click-IT EdU Alexa Fluor 488 Imaging Kit (C10337, Invitrogen). TUNEL assays were performed using *In Situ* Cell Death Detection Kit, Fluorescein (11684795910, Roche). All imaging was done on a Leica fluorescent microscope (Leica DMi8) using Leica Application Suite X software for initial processing. Cell counter plugin of ImageJ was used to quantify cells in images of immunolabeled hCOs.

RAS, Rac1, and RhoA activity assays—For small molecule treatments, 14DIV hCOs were incubated with 10 μM Pan-RAS-IN-1 (HY-101295, MedChemExpress) for 48 hours, and RAS activity (STA-440, Cell Biolabs) was determined on liquid nitrogen snap frozen specimens according to the manufacturer's instructions. NSCs or 8DIV EBs were treated for 24h with 1 μg/ml Rho Activator II (CN-03; Cytoskeleton; CN03) to induce Rho activation. RhoA (BK124, Cytoskeleton) and Rac1 (BK128, Cytoskeleton) activity assays were performed on liquid nitrogen snap frozen NSC and hCO specimens, according to the manufacturer's instructions.

Real-time quantitative PCR—Total RNA was extracted (RNeasy Mini Kit, QIAGEN) from hiPSC-derived hCOs according to manufacturer's instructions. RNA concentrations and purity were assessed using a NanoDrop 2000 Spectrophotometer prior to reverse transcription using a high-capacity cDNA reverse transcription kit (4374966, Applied Biosystems). RT-qPCR was performed using TaqMan gene expression assays [*CRLF3* (Hs00367579_m1), *ATAD5* (Hs00227495_m1), *TEFM* (Hs00895248_m1), *ADAP2* (Hs01106939_m1), *COPRS* (Hs0104 7650_m1), *UTP6* (Hs00251161_m1), *SUZ12* (Hs00248742_m1), *LRRC37B* (Hs03045845_m1), *MIR193A* (Hs04273253_s1), *MIR365B* (Hs04231549_s1), *MIR4725* (Hs06637953_s1), *MIR4733* (Hs04274676_s1)] and TaqMan Fast Advanced Master Mix, no UNG (4444964, Applied Biosystems) according to manufacturer's instructions. All reactions were performed using the Bio-Rad CFX96 Real-Time PCR system equipped with Bio-Rad CFX Manager 3.1 software. Gene expression levels of technical replicates were estimated by ΔΔCt method using GAPDH (Hs02786624_g1) as a reference gene.

Western blot analysis—hCO, NSC and iPSC samples were collected, sonicated in RIPA buffer (89900, Thermo Scientific) containing 2 μg/mL aprotinin (ab146286, Abcam), 10 μg/mL leupeptin (L2884, Sigma-Aldrich), and 1 mM PMSF (10837091001, Sigma-Aldrich), and total protein concentrations determined (Pierce BCA protein assay kit, 23225, Thermo Scientific). Reducing Laemmli buffer (1610747, Bio-Rad) was added and samples incubate at 95°C for 5 minutes. Equal amounts of protein (30 to 45 μg) were loaded into each well of 8% or 10% SDS-PAGE gels and run for 1.5 hours at 120 V, followed by transfer to polyvinylidene fluoride membranes using an Invitrogen power blotting system. The

membranes were blocked for 1 hour in 5% milk in Tris-buffered saline (TBS), followed by incubation overnight at 4°C with primary antibodies in TBS: anti-SUZ12 (1 μg/mL, ab12073, Abcam), anti-COPRS (1:500, NBP2-30884, Novus Biologicals), anti-CRLF3 (1:100, HPA007596, Sigma-Aldrich), anti-ATAD5 (1:500, LS-C19118, Lifespan Biosciences), anti-UTP6 (1:300, 17671-1-AP, Proteintech), anti-N-cadherin (1:1000, ab18203, Abcam), anti-neurofibromin (1:100; unpublished data), anti-Vinculin (1:5000, ab129002, Abcam) and anti-GAPDH (1:2,000, ab8245, Abcam). After washing with TBS, blots were incubated with a 1:5,000 dilution of goat anti-rabbit IRDye 680RD (926-68071, LI-COR Biosciences) and goat anti-mouse IRDye 800CW (925-32210, LI-COR Biosciences) secondary antibodies in TBS for one hour at room temperature. Imaging of immunoblots was performed using a LI-COR Odyssey Fc imaging system (LI-COR Biosciences). Protein bands were quantified using LI-COR Image Studio Software v5.2, and experimental protein values were normalized to GAPDH or Vinculin as an internal loading control.

RNA interference—CTL1 hiPSCs were infected with four independent *CRLF3* shRNA lentiviral particles (sc-94066-V, Santa Cruz Biotechnology; sh*CRLF3* A: AAAGGCTTCGCACATTCAGTTGGACAGCT; sh*CRLF3* B: TACAGTCTGAGCAGTCGAAGAAATATAGC; sh*CRLF3* C: GACATTGAAGCCGTGACTCTAGGAACCAC; TL305215V, Origene) (MOI = 5) or control shRNA lentiviral particles (sc-108080, Santa Cruz Biotechnology; TR30021V shRNA scramble control particles, Origene) (MOI = 5). Infected cultures were incubated with mTeSR Plus medium (05825, STEMCELL Technologies) containing 0.4 μg/mL puromycin (73342, STEMCELL Technologies) for selection, and the medium was replaced every other day until drug-resistant colonies formed (~14 days). Resulting colonies were expanded, assayed for *CRLF3* gene expression by western blotting and were differentiated into NSCs or hCOs.

Ortholog sequence comparison—NCBI's Eukaryotic Genome Annotation pipeline was used to identify vertebrate orthologs of human CRLF3. Amino acid sequence alignments were generated by NCBI's constraint-based multiple alignment tool (Cobalt) that finds a collection of pairwise constraints derived from conserved domain database, protein motif database, and sequence similarity, using RPS-BLAST, BLASTP, and PHIBLAST (Papadopoulos and Agarwala, 2007). Alignment results were visualized by Jalview.

QUANTIFICATION AND STATISTICAL ANALYSIS

No statistical methods were used to predetermine sample size. Sample size was deemed satisfactory based on the magnitude and consistency of differences between groups. No randomization of samples was performed, and investigators were not blinded during experiments and outcome assessment. Image fields for NeuroD1$^+$ neuronal quantifications were selected from the inner subventricular zones of hCOs. Image fields for NeuN$^+$, TBR1$^+$ and SATB2$^+$ neuronal quantifications were selected from the outer subventricular zones of hCOs. The number of biological replicates (hCOs) per independent experimental replicate per genotype is provided in the figure legends. For each genotype, all available clones were analyzed. All statistical analyses were performed using GraphPad Prism 8 software.

Statistical significance was determined using one-way analysis of variance (ANOVA) with Dunnett's multiple comparisons test, Bonferroni multiple comparisons test, Tukey multiple comparison's test, two-way ANOVA with Sidak's multiple comparison test, or unpaired, two-tailed t test. The exact values from the tests are indicated in the figures. Statistical significance was defined as $p < 0.05$. Bar graphs indicate the mean ± SEM. Boxplot indicates median (central line), interquartile range (box) and minimum and maximum values (whiskers).

A summary table summarizing all the experiments is now included in Table S4, discriminating the samples in each figure panel with the statistical methods used for analysis.

Supplementary Material

Refer to Web version on PubMed Central for supplementary material.

ACKNOWLEDGMENTS

We thank Dr. Matthew B. Harms and Dr. Fumihiko Urano (Washington University, St. Louis, MO) for providing neurologically normal control patient-derived hiPSC lines. This work was supported by a Young Investigator's Award grant from the Children's Tumor Foundation (2018-01-003 to M.L.W.) and a Research Program Award grant from the National Institutes of Health (1-R35-NS07211-01 to D.H.G.). The GeiC facility at WUSM engineered the hiPSCs and is subsidized by NCI Cancer Center Support Grant P30-CA091842.

REFERENCES

Abrahams BS, Arking DE, Campbell DB, Mefford HC, Morrow EM, Weiss LA, Menashe I, Wadkins T, Banerjee-Basu S, and Packer A (2013). SFARI Gene 2.0: a community-driven knowledgebase for the autism spectrum disorders (ASDs). Mol. Autism 4, 36. [PubMed: 24090431]

Anastasaki C, Woo AS, Messiaen LM, and Gutmann DH (2015). Elucidating the impact of neurofibromatosis-1 germline mutations on neurofibromin function and dopamine-based learning. Hum. Mol. Genet 24, 3518–3528. [PubMed: 25788518]

Anastasaki C, Wegscheid ML, Hartigan K, Papke JB, Kopp ND, Chen J, Cobb O, Dougherty JD, and Gutmann DH (2020). Human iPSC-derived neurons and cerebral organoids establish differential effects of germline NF1 gene mutations. Stem Cell Reports 14, 541–550. [PubMed: 32243842]

Arikkath J, Peng IF, Ng YG, Israely I, Liu X, Ullian EM, and Reichardt LF (2009). Delta-catenin regulates spine and synapse morphogenesis and function in hippocampal neurons during development. J. Neurosci 29, 5435–5442. [PubMed: 19403811]

Ashburner M, Ball CA, Blake JA, Botstein D, Butler H, Cherry JM, Davis AP, Dolinski K, Dwight SS, Eppig JT, et al.; The Gene Ontology Consortium (2000). Gene ontology: tool for the unification of biology. Nat. Genet 25, 25–29. [PubMed: 10802651]

Banerjee-Basu S, and Packer A (2010). SFARI Gene: an evolving database for the autism research community. Dis. Model. Mech 3, 133–135. [PubMed: 20212079]

Chen YH, Gianino SM, and Gutmann DH (2015). Neurofibromatosis-1 regulation of neural stem cell proliferation and multilineage differentiation operates through distinct RAS effector pathways. Genes Dev. 29, 1677–1682. [PubMed: 26272820]

Coe BP, Stessman HAF, Sulovari A, Geisheker MR, Bakken TE, Lake AM, Dougherty JD, Lein ES, Hormozdiari F, Bernier RA, and Eichler EE (2019). Neurodevelopmental disease genes implicated by de novo mutation and copy number variation morbidity. Nat. Genet 51, 106–116. [PubMed: 30559488]

Constantino JN, Zhang Y, Holzhauer K, Sant S, Long K, Vallorani A, Malik L, and Gutmann DH (2015). Distribution and within-family specificity of quantitative autistic traits in patients with neurofibromatosis type I. J. Pediatr 167, 621–626.e1. [PubMed: 26051969]

De Raedt T, Beert E, Pasmant E, Luscan A, Brems H, Ortonne N, Helin K, Hornick JL, Mautner V, Kehrer-Sawatzki H, et al. (2014). PRC2 loss amplifies Ras-driven transcription and confers sensitivity to BRD4-based therapies. Nature 514, 247–251. [PubMed: 25119042]

Descheemaeker MJ, Roelandts K, De Raedt T, Brems H, Fryns JP, and Legius E (2004). Intelligence in individuals with a neurofibromatosis type 1 microdeletion. Am. J. Med. Genet. A 131, 325–326. [PubMed: 15472997]

Dobin A, Davis CA, Schlesinger F, Drenkow J, Zaleski C, Jha S, Batut P, Chaisson M, and Gingeras TR (2013). STAR: ultrafast universal RNA-seq aligner. Bioinformatics 29, 15–21. [PubMed: 23104886]

Douglas J, Cilliers D, Coleman K, Tatton-Brown K, Barker K, Bernhard B, Burn J, Huson S, Josifova D, Lacombe D, et al.; Childhood Overgrowth Collaboration (2007). Mutations in RNF135, a gene within the NF1 microdeletion region, cause phenotypic abnormalities including overgrowth. Nat. Genet 39, 963–965. [PubMed: 17632510]

Elia LP, Yamamoto M, Zang K, and Reichardt LF (2006). p120 catenin regulates dendritic spine and synapse development through Rho-family GTPases and cadherins. Neuron 51, 43–56. [PubMed: 16815331]

Frega M, Linda K, Keller JM, Gümüş-Akay G, Mossink B, van Rhijn JR, Negwer M, Klein Gunnewiek T, Foreman K, Kompier N, et al. (2019). Neuronal network dysfunction in a model for Kleefstra syndrome mediated by enhanced NMDAR signaling. Nat. Commun 10, 4928. [PubMed: 31666522]

Fukata M, and Kaibuchi K (2001). Rho-family GTPases in cadherin-mediated cell-cell adhesion. Nat. Rev. Mol. Cell Biol 2, 887–897. [PubMed: 11733768]

Gilbert J, and Man HY (2016). The X-linked autism protein KIAA2022/KIDLIA regulates neurite outgrowth via N-cadherin and δ-catenin signaling. eNeuro 3, ENEURO.0238-16.2016.

Grayton HM, Fernandes C, Rujescu D, and Collier DA (2012). Copy number variations in neurodevelopmental disorders. Prog. Neurobiol 99, 81–91. [PubMed: 22813947]

Hahn N, Knorr DY, Liebig J, Wüstefeld L, Peters K, Büscher M, Bucher G, Ehrenreich H, and Heinrich R (2017). The insect ortholog of the human orphan cytokine receptor CRLF3 is a neuroprotective erythropoietin receptor. Front. Mol. Neurosci 10, 223. [PubMed: 28769759]

Hahn N, Büschgens L, Schwedhelm-Domeyer N, Bank S, Geurten BRH, Neugebauer P, Massih B, Göpfert MC, and Heinrich R (2019). The orphan cytokine receptor CRLF3 emerged with the origin of the nervous system and is a neuroprotective erythropoietin receptor in locusts. Front. Mol. Neurosci 12, 251. [PubMed: 31680856]

Hegedus B, Dasgupta B, Shin JE, Emnett RJ, Hart-Mahon EK, Elghazi L, Bernal-Mizrachi E, and Gutmann DH (2007). Neurofibromatosis-1 regulates neuronal and glial cell differentiation from neuroglial progenitors in vivo by both cAMP- and Ras-dependent mechanisms. Cell Stem Cell 1, 443–457. [PubMed: 18371380]

Hutsler JJ, and Zhang H (2010). Increased dendritic spine densities on cortical projection neurons in autism spectrum disorders. Brain Res. 1309, 83–94. [PubMed: 19896929]

Kehrer-Sawatzki H, Mautner VF, and Cooper DN (2017). Emerging genotype-phenotype relationships in patients with large NF1 deletions. Hum. Genet 136, 349–376. [PubMed: 28213670]

Kluwe L, Siebert R, Gesk S, Friedrich RE, Tinschert S, Kehrer-Sawatzki H, and Mautner VF (2004). Screening 500 unselected neurofibromatosis 1 patients for deletions of the NF1 gene. Hum. Mutat 23, 111–116. [PubMed: 14722914]

Lazar M, Miles LM, Babb JS, and Donaldson JB (2014). Axonal deficits in young adults with High Functioning Autism and their impact on processing speed. Neuroimage Clin. 4, 417–425. [PubMed: 24624327]

Lee DY, Yeh TH, Emnett RJ, White CR, and Gutmann DH (2010). Neurofibromatosis-1 regulates neuroglial progenitor proliferation and glial differentiation in a brain region-specific manner. Genes Dev. 24, 2317–2329. [PubMed: 20876733]

Lee W, Teckie S, Wiesner T, Ran L, Prieto Granada CN, Lin M, Zhu S, Cao Z, Liang Y, Sboner A, et al. (2014). PRC2 is recurrently inactivated through EED or SUZ12 loss in malignant peripheral nerve sheath tumors. Nat. Genet 46, 1227–1232. [PubMed: 25240281]

Love MI, Huber W, and Anders S (2014). Moderated estimation of fold change and dispersion for RNA-seq data with DESeq2. Genome Biol. 15, 550. [PubMed: 25516281]

Matter C, Pribadi M, Liu X, and Trachtenberg JT (2009). Delta-catenin is required for the maintenance of neural structure and function in mature cortex in vivo. Neuron 64, 320–327. [PubMed: 19914181]

Mautner VF, Kluwe L, Friedrich RE, Roehl AC, Bammert S, Högel J, Spöri H, Cooper DN, and Kehrer-Sawatzki H (2010). Clinical characterisation of 29 neurofibromatosis type-1 patients with molecularly ascertained 1.4 Mb type-1 NF1 deletions. J. Med. Genet 47, 623–630. [PubMed: 20543202]

Messiaen L, Vogt J, Bengesser K, Fu C, Mikhail F, Serra E, Garcia-Linares C, Cooper DN, Lazaro C, and Kehrer-Sawatzki H (2011). Mosaic type-1 NF1 microdeletions as a cause of both generalized and segmental neurofibromatosis type-1 (NF1). Hum. Mutat 32, 213–219. [PubMed: 21280148]

Morris SM, Acosta MT, Garg S, Green J, Huson S, Legius E, North KN, Payne JM, Plasschaert E, Frazier TW, et al. (2016). Disease burden and symptom structure of autism in neurofibromatosis type 1: a study of the International NF1-ASD Consortium Team (INFACT). JAMA Psychiatry 73, 1276–1284. [PubMed: 27760236]

Mukaetova-Ladinska EB, Arnold H, Jaros E, Perry R, and Perry E (2004). Depletion of MAP2 expression and laminar cytoarchitectonic changes in dorsolateral prefrontal cortex in adult autistic individuals. Neuropathol. Appl. Neurobiol 30, 615–623. [PubMed: 15541002]

Ostrowski D, and Heinrich R (2018). Alternative erythropoietin receptors in the nervous system. J. Clin. Med 7, 24.

Ottenhoff MJ, Rietman AB, Mous SE, Plasschaert E, Gawehns D, Brems H, Oostenbrink R, ENCORE-NF1 Team; van Minkelen R, Nellist M, et al. (2020). Examination of the genetic factors underlying the cognitive variability associated with neurofibromatosis type 1. Genet. Med 22, 889–897. [PubMed: 32015538]

Papadopoulos JS, and Agarwala R (2007). COBALT: constraint-based alignment tool for multiple protein sequences. Bioinformatics 23, 1073–1079. [PubMed: 17332019]

Partek Inc (2020). Partek Flow software, version 9.0 (St. Louis, MO: Partek Inc.).

Pasmant E, Sabbagh A, Spurlock G, Laurendeau I, Grillo E, Hamel MJ, Martin L, Barbarot S, Leheup B, Rodriguez D, et al.; Members of the NF France Network (2010). NF1 microdeletions in neurofibromatosis type 1: from genotype to phenotype. Hum. Mutat 31, E1506–E1518. [PubMed: 20513137]

Pucilowska J, Vithayathil J, Pagani M, Kelly C, Karlo JC, Robol C, Morella I, Gozzi A, Brambilla R, and Landreth GE (2018). Pharmacological inhibition of ERK signaling rescues pathophysiology and behavioral phenotype associated with 16p11.2 chromosomal deletion in mice. J. Neurosci 38, 6640–6652. [PubMed: 29934348]

Ramocki MB, Bartnik M, Szafranski P, Kołodziejska KE, Xia Z, Bravo J, Miller GS, Rodriguez DL, Williams CA, Bader PI, et al. (2010). Recurrent distal 7q11.23 deletion including HIP1 and YWHAG identified in patients with intellectual disabilities, epilepsy, and neurobehavioral problems. Am. J. Hum. Genet 87, 857–865. [PubMed: 21109226]

Rasmussen SA, Colman SD, Ho VT, Abernathy CR, Arn PH, Weiss L, Schwartz C, Saul RA, and Wallace MR (1998). Constitutional and mosaic large NF1 gene deletions in neurofibromatosis type 1. J. Med. Genet 35, 468–471. [PubMed: 9643287]

Richter M, Murtaza N, Scharrenberg R, White SH, Johanns O, Walker S, Yuen RKC, Schwanke B, Bedürftig B, Henis M, et al. (2019). Altered TAOK2 activity causes autism-related neurodevelopmental and cognitive abnormalities through RhoA signaling. Mol. Psychiatry 24, 1329–1350. [PubMed: 29467497]

Sanchez-Ortiz E, Cho W, Nazarenko I, Mo W, Chen J, and Parada LF (2014). NF1 regulation of RAS/ERK signaling is required for appropriate granule neuron progenitor expansion and migration in cerebellar development. Genes Dev. 28, 2407–2420. [PubMed: 25367036]

Shcheglovitov A, Shcheglovitova O, Yazawa M, Portmann T, Shu R, Sebastiano V, Krawisz A, Froehlich W, Bernstein JA, Hallmayer JF, and Dolmetsch RE (2013). SHANK3 and IGF1 restore synaptic deficits in neurons from 22q13 deletion syndrome patients. Nature 503, 267–271. [PubMed: 24132240]

Sloan SA, Andersen J, Paşca AM, Birey F, and Paşca SP (2018). Generation and assembly of human brain region-specific three-dimensional cultures. Nat. Protoc 13, 2062–2085. [PubMed: 30202107]

Tan ZJ, Peng Y, Song HL, Zheng JJ, and Yu X (2010). N-cadherin-dependent neuron-neuron interaction is required for the maintenance of activity-induced dendrite growth. Proc. Natl. Acad. Sci. USA 107, 9873–9878. [PubMed: 20457910]

Tastet J, Decalonne L, Marouillat S, Malvy J, Thépault RA, Toutain A, Paubel A, Tabagh R, Bénédetti H, Laumonnier F, et al. (2015). Mutation screening of the ubiquitin ligase gene RNF135 in French patients with autism. Psychiatr. Genet 25, 263–267. [PubMed: 26368817]

Turner TN, Sharma K, Oh EC, Liu YP, Collins RL, Sosa MX, Auer DR, Brand H, Sanders SJ, Moreno-De-Luca D, et al. (2015). Loss of δ-catenin function in severe autism. Nature 520, 51–56. [PubMed: 25807484]

Venturin M, Guarnieri P, Natacci F, Stabile M, Tenconi R, Clementi M, Hernandez C, Thompson P, Upadhyaya M, Larizza L, and Riva P (2004). Mental retardation and cardiovascular malformations in NF1 microdeleted patients point to candidate genes in 17q11.2. J. Med. Genet 41, 35–41. [PubMed: 14729829]

Venturin M, Carra S, Gaudenzi G, Brunelli S, Gallo GR, Moncini S, Cotelli F, and Riva P (2014). ADAP2 in heart development: a candidate gene for the occurrence of cardiovascular malformations in NF1 microdeletion syndrome. J. Med. Genet 51, 436–443. [PubMed: 24711647]

Wang Y, Kim E, Wang X, Novitch BG, Yoshikawa K, Chang LS, and Zhu Y (2012). ERK inhibition rescues defects in fate specification of Nf1-deficient neural progenitors and brain abnormalities. Cell 150, 816–830. [PubMed: 22901811]

Wassef M, Luscan A, Aflaki S, Zielinski D, Jansen PWTC, Baymaz HI, Battistella A, Kersouani C, Servant N, Wallace MR, et al. (2019). EZH1/2 function mostly within canonical PRC2 and exhibit proliferation-dependent redundancy that shapes mutational signatures in cancer. Proc. Natl. Acad. Sci. USA 116, 6075–6080. [PubMed: 30867289]

Wolff JJ, Gu H, Gerig G, Elison JT, Styner M, Gouttard S, Botteron KN, Dager SR, Dawson G, Estes AM, et al.; IBIS Network (2012). Differences in white matter fiber tract development present from 6 to 24 months in infants with autism. Am. J. Psychiatry 169, 589–600. [PubMed: 22362397]

World Health Organization (2017). Global accelerated action for the health of adolescents (AA-HA!): guidance to support country implementation: summary (Geneva: World Health Organization).

Yang F, Xu YP, Li J, Duan SS, Fu YJ, Zhang Y, Zhao Y, Qiao WT, Chen QM, Geng YQ, et al. (2009). Cloning and characterization of a novel intracellular protein p48.2 that negatively regulates cell cycle progression. Int. J. Biochem. Cell Biol 41, 2240–2250. [PubMed: 19427400]

Zhang M, Wang Y, Jones S, Sausen M, McMahon K, Sharma R, Wang Q, Belzberg AJ, Chaichana K, Gallia GL, et al. (2014). Somatic mutations of SUZ12 in malignant peripheral nerve sheath tumors. Nat. Genet 46, 1170–1172. [PubMed: 25305755]

Highlights

- Increased NSC proliferation in *NF1*-TGD hCOs is RAS-dependent
- *NF1*-TGD hCOs have elevated neuronal survival and maturation deficits
- Increased neuronal death and dendritic deficits in *NF1*-TGD hCOs are *CRLF3*-dependent
- RhoA activation rescues neuronal survival and maturation deficits in *NF1*-TGD hCOs

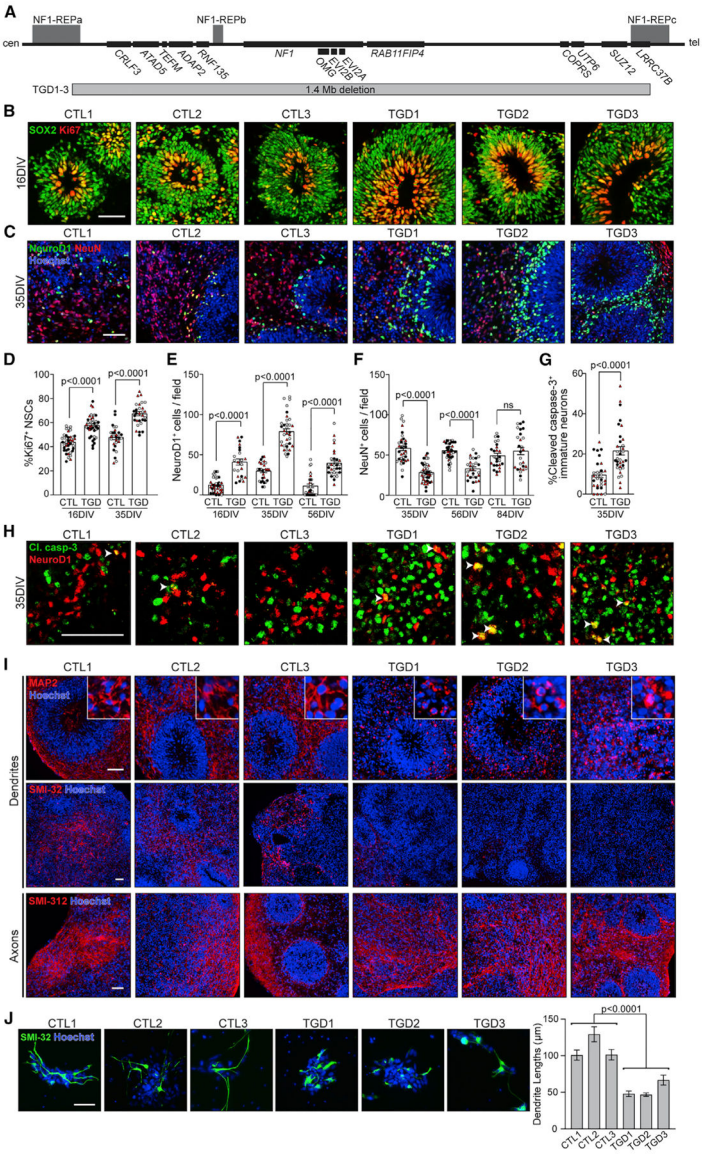

Figure 1. TGD hCOs and neurons exhibit neuronal defects

(A) Protein-coding genes within the 17q11.2 microdeletion region, denoting the length and location of the 1.4-Mb deletion (adapted from Kehrer-Sawatzki et al. [2017]).

(B and D) Images and quantification of VZ NSC proliferation ($Ki67^+$, red) in control (CTL) and TGD hCOs at 16 and 35 DIV.

(C) Images of 35 DIV hCOs immunolabeled for $NeuroD1^+$ (green) and $NeuN^+$ (red) neuronal markers.

(E and F) Number of (E) $NeuroD1^+$ and (F) $NeuN^+$ neurons per image field in the SVZs of TGD hCOs relative to CTL.

(G) Increased apoptotic immature neurons in TGD hCOs compared to CTL at 35 DIV.

(D–G) Each data point represents 1 hCO, 2–6 hCOs per experimental replicate, and 3–5 experimental replicates per genotype. Independent hiPSC lines representing three different

CTL or TGD lines (black, CTL1/ TGD1; white, CTL2/ TGD2; red, CTL3/ TGD3) are shown.

(H) White arrowheads indicate co-localization of NeuroD1$^+$ neurons (red) and cleaved caspase-3 (green) in CTL and TGD hCOs at 35 DIV.

(I) Images of hCOs immunolabeled for dendrites (MAP2$^+$, SMI-32$^+$) and axons (SMI-312$^+$) at 35 DIV.

(J) Images of 2D CTL and TGD neurons immunolabeled for SMI-32, with a graph depicting the mean dendrite lengths per genotype.

Three independent experimental replicates per genotype, 48–112 neurites per replicate. Data are shown as the mean ± SEM. Statistical analyses by unpaired (D–G) two-tailed t test or (J) one-way ANOVA. Scale bars: (B–I) 50 μm; (J) 100 μm.

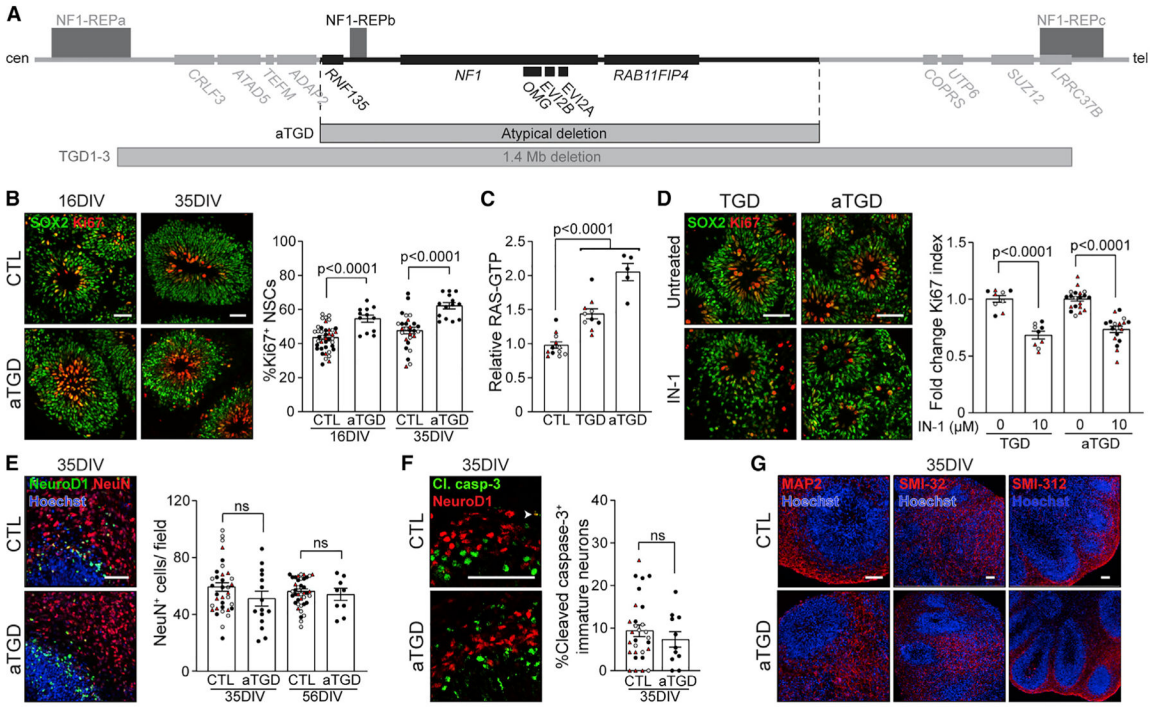

Figure 2. RAS hyperactivation drives the increased NSC proliferation in TGD hCOs

(A) Diagram illustrating the 1.4-Mb (TGD) and atypical (aTGD) microdeletions, highlighting their commonly deleted region.

(B) Images and quantification of NSC ($SOX2^+$) proliferation ($Ki67^+$) in CTL and aTGD hCOs at 16 and 35 DIV.

(C) TGD and aTGD hCOs have increased RAS activity relative to CTL hCOs at 16 DIV. Each data point represents an independent experimental replicate consisting of 4 pooled hCOs.

(D) Images and quantification of NSC proliferation (fold change in $\%Ki67^+$ NSCs) in three clones of TGD and aTGD hCOs at 16 DIV with or without IN-1 treatment.

(E–G) Images and quantification of CTL and aTGD hCOs showing normal (E) production of $NeuN^+$ neurons at 35 and 56 DIV, (F) early-stage immature neuron apoptosis, and (G) production of dendrites ($MAP2^+$, $SMI\text{-}32^+$) and axons ($SMI\text{-}312^+$) at 35 DIV.

(B and D–F) Each data point represents 1 hCO, 2–6 hCOs per experimental replicate, 3–5 experimental replicates per genotype. Independent hiPSC lines representing three different CTL or aTGD lines (black, CTL1/ aTGD1; white, CTL2/ aTGD2; red, CTL3/ aTGD3) are shown. All data are shown as the mean ± SEM. Statistical analysis by one-way ANOVA with Dunnett's multiple-comparisons test or unpaired, two-tailed t test. Scale bars: 50 μm.

B

	mRNA expression												Protein expression									
	CTL			TGD				aTGD					CTL			TGD				aTGD			
Gene	Mean	SD	N	Mean	SD	N	P value	Mean	SD	N	P value		Mean	SD	N	Mean	SD	N	P value	Mean	SD	N	P value
CRLF3	1.00	0.37	19	0.47	0.19	23	<0.0001	1.10	0.16	13	0.3706		1.00	0.32	13	0.34	0.12	11	<0.0001	1.92	0.55	4	<0.0001
ATAD5	1.00	0.26	17	0.41	0.17	17	<0.0001	1.37	0.66	13	0.0412		1.00	0.33	15	1.22	0.56	15	0.1941	0.99	0.27	5	0.9534
TEFM	1.00	0.34	18	0.52	0.22	23	<0.0001	1.53	0.35	13	0.0002							*					
COPRS	1.00	0.38	18	0.35	0.12	20	<0.0001	1.21	0.22	13	0.0881		1.00	0.36	12	2.52	3.19	12	0.1143	0.59	0.17	5	0.0284
UTP6	1.00	0.43	21	0.40	0.17	20	<0.0001	0.79	0.28	13	0.1379		1.00	0.23	12	1.12	0.38	12	0.3638	0.97	0.08	4	0.8313
SUZ12	1.00	0.32	22	0.50	0.20	21	<0.0001	0.92	0.17	13	0.3848		1.00	0.33	10	0.73	0.23	9	0.0863	1.15	0.17	5	0.3525
LRRC37B	1.00	0.47	19	0.54	0.47	23	0.0032	1.09	0.31	13	0.5417							*					

*no antibody available

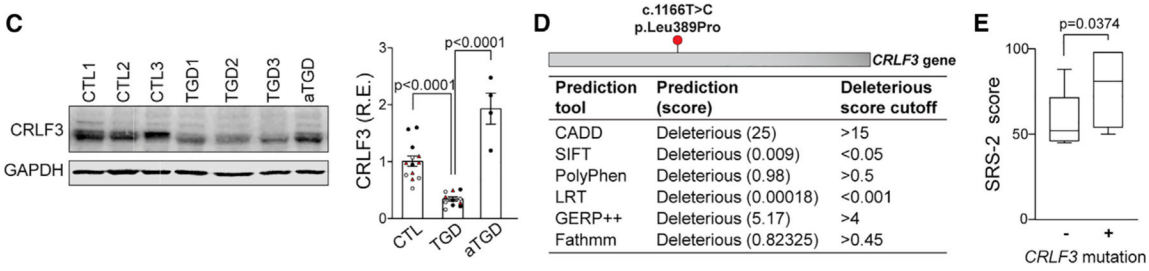

Figure 3. *CRLF3* is uniquely disrupted in TGD hCOs and NF1 patients with increased SRS-2 scores

(A) 17q11.2 region highlighting the loci uniquely deleted in TGD microdeletions and the *CRLF3* gene (red).

(B) mRNA and protein expression analysis at 56 DIV of protein-coding genes uniquely deleted in TGD hCOs. Each mRNA data point represents 1 hCO, 3 hCOs per experimental replicate. Each protein data point represents an independent replicate consisting of 4 pooled hCOs.

(C) Western blot and quantification demonstrating reduced CRLF3 protein levels in TGD relative to CTL and aTGD 56 DIV hCOs. Data are shown as the mean ± SEM. Independent hiPSC lines representing 3 different CTL or TGD lines (black, CTL1/ TGD1; white, CTL2/ TGD2; red, CTL3/ TGD3) are shown.

(D) Position of the deleterious *CRLF3* c.1166T>C mutation found in 7/17 NF1 patients, with mutational effect predictions using six methods.

(E) NF1 patients with the *CRLF3* c.1166T>C mutation (n = 7) have higher SRS-2 scores than those without it (n = 10). Boxplot indicates median (central line), interquartile range (box), and minimum and maximum values (whiskers).

(C and E) Statistical analysis by unpaired, two-tailed t test.

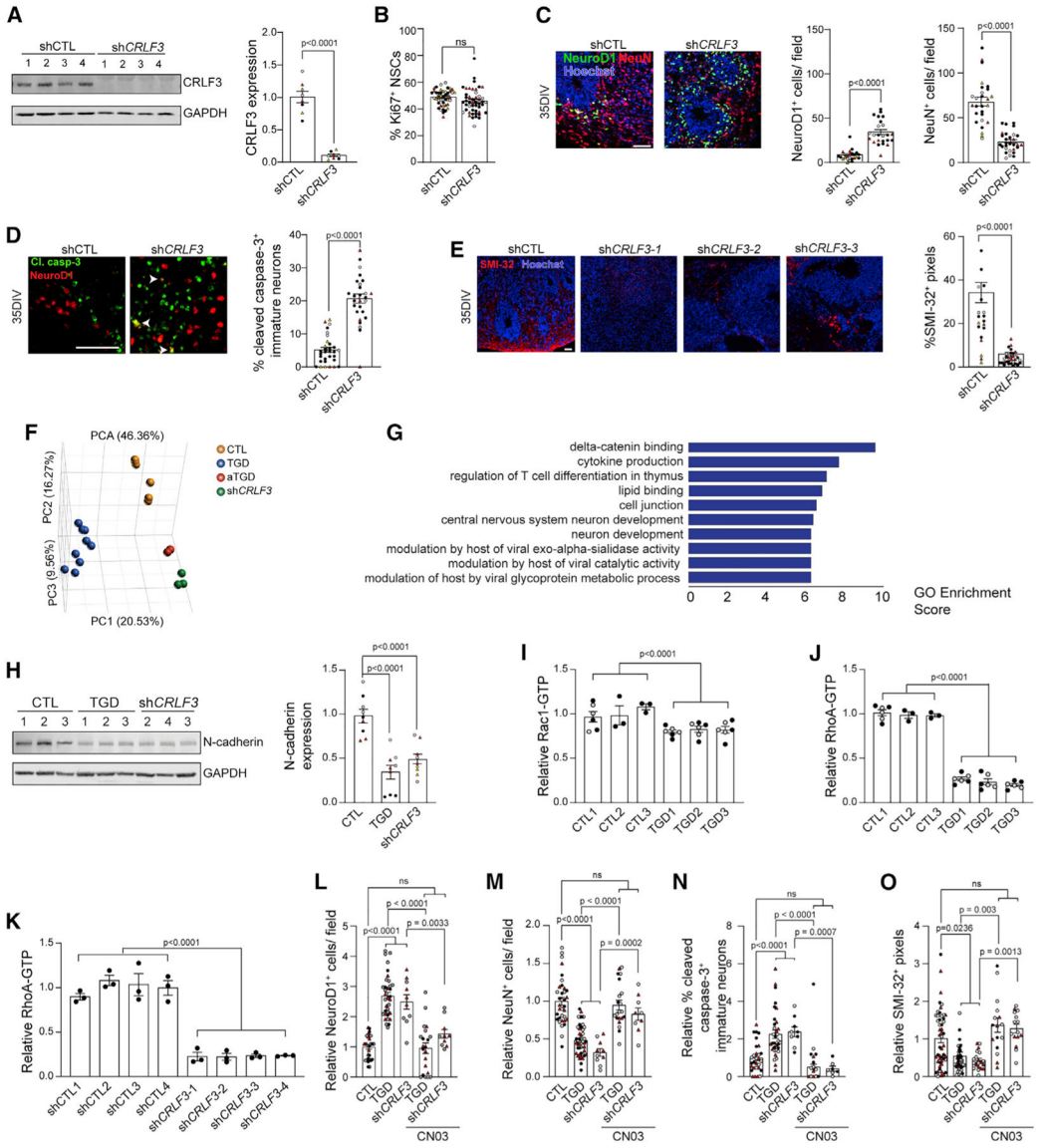

Figure 4. Impaired RhoA signaling drives *CRLF3*-mediated neuronal defects

(A)Western blot showing reduced CRLF3 protein levels in CTL1 hiPSCs infected with sh*CRLF3* constructs relative to shCTL.

(B) NSC proliferation (%Ki67$^+$ NSCs) in 16 DIV hCOs from shCTL and sh*CRLF3* lines.

(C–E) Images and quantification of shCTL and sh*CRLF3* hCOs showing (C) increased production of NeuroD1$^+$ (green) neurons and reduced NeuN$^+$ (red) neurons, (D) increased apoptotic (Cl. casp-3, green) immature (NeuroD1, red) neurons, and (E) reduced SMI-32$^+$ dendrites in sh*CRLF3* compared to shCTL hCOs. Each data point represents 1 hCO, 3–10 hCOs per hiPSC line. Statistical analysis by unpaired, two-tailed t test.

(F) Principal component analysis showing distinct transcriptional profiles in CTL, TGD, aTGD, and sh*CRLF3* NSCs.

(G) Enrichment scores of the top 10 gene ontologies (p value ≤ 0.01) in sh*CRLF3* and TGD relative to CTL and aTGD NSCs.

(H) Western blot and quantification of N-cadherin protein levels in CTL, TGD, and sh*CRLF3* NSCs. n = 3 biological replicates per genotype. Statistical analysis by one-way ANOVA with Dunnett's multiple-comparisons test.

(I–K) Rac1 (I) and RhoA (J and K) activity levels in CTL and TGD (J) or shCTL and sh*CRLF3* (K) NSCs. Each data point represents an independently generated biological replicate, 3 biological replicates per genotype. Statistical analysis by unpaired, two-tailed t test.

(L–O) Quantitation of (L) NeuroD1$^+$ neurons, (M) NeuN$^+$ neurons, (N) cl. Caspase-3+ apoptotic immature neurons, and (O) SMI-32$^+$ immunopositive dendrites in 35 DIV TGD and *shCRLF3 hCOs* with and without CN03 treatment relative to control hCOs. Data are represented as fold-change relative to controls. Each data point represents 1 hCO, 2–6 hCOs per experimental replicate, and 3–5 experimental replicates per genotype.

(A–O) All data are shown as the mean ± SEM. Independent hiPSC lines representing (A–D) four different shCTL or sh*CRLF3* lines (black, shCTL1/sh*CRLF3*-1; white, shCTL2/sh*CRLF3*-2; red, shCTL3/sh*CRLF3*-3; yellow, shCTL4/sh*CRLF3*-4), (H and L–O) three different CTL, TGD, or sh*CRLF3* lines (black, CTL1/TGD1/sh*CRLF3*-1; white, CTL2/TGD2/sh*CRLF3*-2; red, CTL3/TGD3/sh*CRLF3*-3), or (I and J) two different clones for each line (black, clone 1; gray, clone 2) are shown. Scale bars: 50 μm.

KEY RESOURCES TABLE

REAGENT or RESOURCE	SOURCE	IDENTIFIER
Antibodies		
Mouse monoclonal anti-SOX2	Cell Signaling Technology	Cat# 4900; RRID: AB_10560516
Rabbit monoclonal anti-SOX2	Abcam	Cat# ab92494; RRID: AB_10585428
Rabbit monoclonal anti-Oct-4A	Cell Signaling Technology	Cat# 2840; RRID: AB_2167691
Rabbit polyclonal anti-Nanog	Cell Signaling Technology	Cat# 3580; RRID: AB_2150399
Mouse monoclonal anti-SMI-32	Biolegend	Cat# 801701; RRID: AB_2564642
Mouse monoclonal anti-SMI-312	Biolegend	Cat# 837904; RRID: AB_2566782
Rabbit monoclonal anti-NeuroD1	Abcam	Cat# ab205300
Mouse monoclonal anti-NeuroD1	Abcam	Cat# ab60704; RRID: AB_943491
Mouse monoclonal anti-NeuN	Millipore	Cat# MAB377; RRID: AB_2298772
Mouse monoclonal anti-Ki-67	BD Biosciences	Cat# 556003; RRID: AB_396287
Mouse monoclonal anti-MAP2 [HM-2]	Abcam	Cat# ab11267; RRID: AB_297885
Rabbit monoclonal anti-Cleaved Caspase-3 (Asp175) (5A1E)	Cell Signaling Technology	Cat# 9664; RRID: AB_2070042
Rabbit polyclonal anti-active Caspase-3	R&D systems	Cat# AF835; RRID: AB_2243952
Goat anti-Rabbit IgG (H+L) Secondary Antibody, Alexa Fluor 488	Thermo Fisher Scientific	Cat# A-11034; RRID: AB_2576217
Goat Anti-Mouse IgG (H+L) Secondary Antibody, Alexa Fluor 488	Thermo Fisher Scientific	Cat# A-11029; RRID: AB_138404
Goat Anti-Rabbit IgG (H+L) Secondary Antibody, Alexa Fluor 568	Thermo Fisher Scientific	Cat# A-11011; RRID: AB_143157
Goat Anti-Mouse IgG (H+L) Secondary Antibody, Alexa Fluor 568	Thermo Fisher Scientific	Cat# A-11004; RRID: AB_2534072
Rabbit polyclonal anti-SUZ12	Abcam	Cat# ab12073; RRID: AB_442939
Rabbit polyclonal anti-COPRS	Novus Biologicals	Cat# NBP2-30884
Rabbit polyclonal anti-CRLF3	Sigma-Aldrich	Cat# HPA007596; RRID: AB_1847241
Rabbit polyclonal anti-ATAD5	Lifespan Biosciences	Cat# LS-C19118-100; RRID: AB_1569353
Rabbit polyclonal anti-UTP6	Proteintech	Cat# 17671-1-AP; RRID: AB_2214465
Mouse monoclonal anti-GAPDH [6C5]	Abcam	Cat# ab8245; RRID: AB_2107448
IRDye 680RD Goat anti-Rabbit IgG antibody	LI-COR Biosciences	Cat# 926-68071; RRID: AB_10956166
IRDye 800CW Goat anti-Mouse IgG antibody	LI-COR Biosciences	Cat# 925-32210; RRID: AB_2687825
Rabbit monoclonal anti-PAX6	Abcam	Cat# ab19504; RRID: RRID:AB_2750924
Mouse monoclonal anti-OTX2	Thermo Fisher Scientific	Cat# MA5-15854; RRID:AB_11155193
Rabbit polyclonal anti-EN1	Thermo Fisher Scientific	Cat# PA5-14149; RRID:AB_2231168
Mouse monoclonal anti-GBX2	Lifespan Biosciences	Cat# LS-C197281; NA
Rabbit monoclonal anti-TBR1	Abcam	Cat# ab31940; RRID:AB_2200219
Mouse monoclonal anti-SATB2	Abcam	Cat# ab51502; RRID:AB_882455
Rabbit polyclonal anti-N-cadherin	Abcam	Cat# ab18203; RRID:AB_444317
Mouse monoclonal anti-Neurofibromin	Unpublished data	N/A
Rabbit polyclonal anti-Nestin	Abcam	Cat# ab92391; RRID:AB_10561437
Rabbit monoclonal anti-Vimentin	Cell Signaling Technology	Cat# 5741; RRID:AB_10695459
Rabbit monoclonal Anti-Vinculin	Abcam	Cat# ab129002; RRID:AB_11144129

REAGENT or RESOURCE	SOURCE	IDENTIFIER
Mouse monoclonal anti-neurofibromin	proprietary	N/A
Bacterial and virus strains		
CRLF3 shRNA lentiviral particles	Santa Cruz Biotechnology	Cat# sc-94066-V
Control shRNA lentiviral particles	Santa Cruz Biotechnology	Cat# sc-108080
CRLF3-Human shRNA lentiviral particles (4 unique 29-mer target-specific shRNA, 1 scramble control)	OriGene Technologies	Cat# TL305215V
Control Lenti particles, scrambled shRNA	OriGene Technologies	Cat# TR30021V
Chemicals, peptides, and recombinant proteins		
Matrigel® Basement Membrane Matrix	Corning	Cat# 354234
mTeSR Plus	STEMCELL Technologies	Cat# 05825
ReLeSR	STEMCELL technologies	Cat# 05873
STEMdiff Neural Induction Medium	STEMCELL technologies	Cat# 05835
Recombinant Human FGF-basic (154 a.a.)	PeproTech	Cat# 100-18B
Y27632 RHO/ROCK pathway inhibitor	STEMCELL technologies	Cat# 72307
GIBCO B-27 Plus Supplement (50X)	Thermo Fisher Scientific	Cat# A3582801
GIBCO Neurobasal Medium	Thermo Fisher Scientific	Cat# 21-103-049
GIBCO DMEM/F-12, HEPES	Thermo Fisher Scientific	Cat# 11330057
GIBCO N-2 Supplement (100X)	Thermo Fisher Scientific	Cat# 17502001
Human recombinant insulin	Sigma-Aldrich	Cat# I2643-25MG
GIBCO Penicillin-Streptomycin (5,000 U/mL)	Thermo Fisher Scientific	Cat# 15070063
RIPA Lysis and Extraction Buffer	Thermo Fisher Scientific	Cat# 89900
GIBCO MEM Non-Essential Amino Acids Solution (100X)	Thermo Fisher Scientific	Cat# 11140050
GIBCO GlutaMax Supplement	Thermo Fisher Scientific	Cat# 35050061
2-Mercaptoethanol	Sigma-Aldrich	Cat# M6250
Recombinant Human Erythropoietin/EPO (Tissue Culture Grade)	R&D Systems	Cat# 287-TC-500
Triton X-100	Sigma-Aldrich	Cat# X100
Shandon Immu-Mount	Thermo Fisher Scientific	Cat# 9990402
Tissue-Tek® O.C.T. Compound, Sakura® Finetek	Electron Microscopy Sciences	Cat# 4583
Hoechst 33258, Pentahydrate (bis-Benzimide)	Thermo Fisher Scientific	Cat# H3569
Pan-RAS-IN-1	MedChemExpress	Cat# HY-101295
4x Laemmli Sample Buffer	Bio-Rad	Cat# 1610747
Aprotinin, serine protease inhibitor	Abcam	Cat# ab146286
Leupeptin	Sigma-Aldrich	Cat# L2884
PMSF	Sigma-Aldrich	Cat# 10837091001
Puromycin	STEMCELL Technologies	Cat# 73342
GIBCO Goat serum	Thermo Fisher Scientific	Cat# 16210064
Poly-L-Ornithine Solution (0.01%)	Sigma-Aldrich	Cat# A-004-C
CellAdhere Laminin-521	STEMCELL Technologies	Cat# 77003
SB 431542	Tocris	Cat# 1614
Compound E	STEMCELL Technologies	Cat# 73952
Dorsomorphin	Abcam	Cat# ab120843
Recombinant Human LIF	PeproTech	Cat# 300-05

REAGENT or RESOURCE	SOURCE	IDENTIFIER
Accutase® Cell Detachment Solution	Fisher Scientific	Cat# MT25058CI
RhoA activator CN03A	Cytoskeleton	Cat# NC0272107
Recombinant Human/Murine/Rat BDNF	PeproTech	Cat# 450-02
Recombinant Human IGF-I	PeproTech	Cat# 100-11
Human Recombinant GDNF	STEMCELL Technologies	Cat# 78058
Dibutyryl-cAMP, sodium salt 250mg	PeproTech	Cat# 1698950
Critical commercial assays		
Click-iT EdU Cell Proliferation Kit for Imaging, Alexa Fluor 488 dye	Thermo Fisher Scientific	Cat# C10337
In Situ Cell Death Detection Kit, Fluorescein	Sigma-Aldrich	Cat# 11684795910
Ras Activation ELISA, Colorimetric	Cell Biolabs	Cat# STA-440
RNeasy Mini Kit	QIAGEN	Cat# 74104
Applied Biosystems High-Capacity cDNA Reverse Transcription Kit with RNase Inhibitor	Thermo Fisher Scientific	Cat# 4374966
Applied Biosystems TaqMan Fast Advanced Master Mix, no UNG	Thermo Fisher Scientific	Cat# A44359
Pierce BCA Protein Assay Kit	Thermo Fisher Scientific	Cat# 23225
RhoA G-LISA Activation Assay, colorimetric	Cytoskeleton	Cat# BK124
Rac1 G-LISA Activation Assay, colorimetric	Cytoskeleton	Cat# BK128
Deposited data		
Whole exome sequencing data	This paper	SRA: PRJNA698597
RNA sequencing data	This paper	GEO: GSE166080
Human RNA-seq time-series of the development of seven major organs	Expression Atlas	https://www.ebi.ac.uk/gxa/experiments/E-MTAB-6814/Results
Experimental models: Cell lines		
BJFF.6 (CTL1) hiPSCs	GeiC – Washington University	RRID: CVCL_VU02
TGD1 hiPSCs	This paper	N/A
TGD2 hiPSCs	This paper	N/A
TGD3 hiPSCs	This paper	N/A
aTGD hiPSCs	This paper	N/A
shCTL1 hiPSCs	This paper	N/A
shCTL2 hiPSCs	This paper	N/A
shCTL3 hiPSCs	This paper	N/A
shCTL4 hiPSCs	This paper	N/A
sh*CRLF3*-1 hiPSCs	This paper	N/A
sh*CRLF3*-2 hiPSCs	This paper	N/A
sh*CRLF3*-3 hiPSCs	This paper	N/A
sh*CRLF3*-4 hiPSCs	This paper	N/A
c.1149C > A *NF1*-mutant hiPSCs	Anastasaki et al., 2020	N/A
c.1185+1G > A *NF1*-mutant hiPSCs	Anastasaki et al., 2020	N/A
c.3431-32_dupGT *NF1*-mutant hiPSCs	Anastasaki et al., 2020	N/A
c.5425C > T *NF1*-mutant hiPSCs	Anastasaki et al., 2020	N/A
c.6619C > T *NF1*-mutant hiPSCs	Anastasaki et al., 2020	N/A

REAGENT or RESOURCE	SOURCE	IDENTIFIER
CTL2 hiPSCs	GeiC – Washington University (Dr. Matthew B. Harms)	N/A
CTL3 hiPSCs	GeiC – Washington University (Dr. Fumihiko Urano)	N/A
Oligonucleotides		
Human *CRLF3* - TaqMan® Gene Expression Assay FAM-MGB	Thermo Fisher Scientific	Hs00367579_m1
Human *ATAD5* TaqMan® Gene Expression Assay FAM-MGB	Thermo Fisher Scientific	Hs00227495_m1
Human *TEFM* TaqMan® Gene Expression Assay FAM-MGB	Thermo Fisher Scientific	Hs00895248_m1
Human *ADAP2* TaqMan® Gene Expression Assay FAM-MGB	Thermo Fisher Scientific	Hs01106939_m1
Human *COPRS* TaqMan® Gene Expression Assay FAM-MGB	Thermo Fisher Scientific	Hs01047650_m1
Human *UTP6* TaqMan® Gene Expression Assay FAM-MGB	Thermo Fisher Scientific	Hs00251161_m1
Human *SUZ12* TaqMan® Gene Expression Assay FAM-MGB	Thermo Fisher Scientific	Hs00248742_m1
Human *LRRC37B* TaqMan® Gene Expression Assay FAM-MGB	Thermo Fisher Scientific	Hs03045845_m1
Human *MIR193A* TaqMan® Gene Expression Assay FAM-MGB	Thermo Fisher Scientific	Hs04273253_s1
Human *MIR365B* TaqMan® Gene Expression Assay FAM-MGB	Thermo Fisher Scientific	Hs04231549_s1
Human *MIR4725* TaqMan® Gene Expression Assay FAM-MGB	Thermo Fisher Scientific	Hs06637953_s1
Human *MIR4733* TaqMan® Gene Expression Assay FAM-MGB	Thermo Fisher Scientific	Hs04274676_s1
Human *GAPDH* TaqMan® Gene Expression Assay FAM-MGB	Thermo Fisher Scientific	Hs02786624_g1
Software and algorithms		
Samtools 1.4.1	http://samtools.sourceforge.net/	RRID: SCR_002105
SnpEff	http://snpeff.sourceforge.net/	RRID: SCR_005191
Combined Annotation Dependent Depletion (CADD)	https://cadd.gs.washington.edu/	RRID: SCR_018393
SIFT	https://sift.bii.a-star.edu.sg/	RRID: SCR_012813
PolyPhen: Polymorphism Phenotyping	http://genetics.bwh.harvard.edu/pph2/	RRID: SCR_013189
Likelihood ratio test (LRT)	http://www.genetics.wustl.edu/jflab/lrt_query.html	N/A
GERP++	http://mendel.stanford.edu/SidowLab/downloads/gerp/	RRID: SCR_000563
Fathmm	http://fathmm.biocompute.org.uk/fathmm-xf/about.html	N/A

REAGENT or RESOURCE	SOURCE	IDENTIFIER
Leica Application Suite X software	https://www.bio-rad.com/enus/sku/1845000-cfx-managersoftware?ID=1845000	RRID: SCR_013673
ImageJ/ Fiji v1.8	https://fiji.sc	RRID: SCR_002285
Bio-Rad CFX Manager 3.1	https://www.bio-rad.com/enus/sku/1845000-cfx-managersoftware?ID=1845000	N/A
LI-COR Image Studio Software v5.2	https://www.licor.com/bio/image-studio/	RRID: SCR_015795
COBALT: Constraint-based Multiple Alignment Tool	https://www.ncbi.nlm.nih.gov/tools/cobalt/cobalt.cgi?link_loc=BlastHomeAd	RRID: SCR_004152
GraphPad Prism 8	https://www.graphpad.com:443/	RRID: SCR_002798
Adobe Illustrator 2020	https://www.adobe.com/products/illustrator.html	RRID: SCR_010279
Adobe Photoshop 2020	https://www.adobe.com/products/photoshop.html	RRID: SCR_014199
Jalview	http://www.jalview.org/	RRID: SCR_006459
Samtools	http://samtools.sourceforge.net/	RRID:SCR_002105
bcl2fastq	https://support.illumina.com/sequencing/sequencing_software/bcl2fastq-conversion-software.html	RRID:SCR_015058
STAR version 2.7.3a	https://github.com/alexdobin/STAR	RRID:SCR_015899
Ensembl	http://www.ensembl.org//useast.ensembl.org/?redirectsrc=//www.ensembl.org%2F	RRID:SCR_002344
DESeq2	https://bioconductor.org/packages/release/bioc/html/DESeq2.html	RRID:SCR_015687
Partek Flow software, version 9.0.20	https://www.partek.com/?q=partekgs	RRID:SCR_011860
Gene Ontology enrichment	http://geneontology.org/	RRID:SCR_002811
Other		
Corning® Costar® Ultra-Low Attachment 96 well round bottom plate	Sigma-Aldrich	Cat# CLS7007
Corning® Costar® Ultra-Low Attachment 24 well plate	Sigma-Aldrich	Cat# CLS3473
25cm^2 Tissue Culture Flask - Vent Cap, Sterile	CELLTREAT	Cat# 229331
6 Well Tissue Culture Plate, Sterile	Celltreat	Cat# 229106